Characterization of δ-PuGa (1 at%. Ga) Oxidation Under Dry Oxygen Atmosphere Exposure

N. Favart, B. Ravat, L. Jolly, I. Zacharie-Aubrun, P.M. Martin, D. Menut, I. Popa, B. Oudot

▶ **To cite this version:**

N. Favart, B. Ravat, L. Jolly, I. Zacharie-Aubrun, P.M. Martin, et al.. Characterization of δ-PuGa (1 at%. Ga) Oxidation Under Dry Oxygen Atmosphere Exposure. High Temperature Corrosion of Materials, 2024, 101, pp.885-896. 10.1007/s11085-024-10267-6 . hal-04703324

HAL Id: hal-04703324
https://hal.science/hal-04703324v1

Submitted on 25 Oct 2024

HAL is a multi-disciplinary open access archive for the deposit and dissemination of scientific research documents, whether they are published or not. The documents may come from teaching and research institutions in France or abroad, or from public or private research centers.

L'archive ouverte pluridisciplinaire **HAL**, est destinée au dépôt et à la diffusion de documents scientifiques de niveau recherche, publiés ou non, émanant des établissements d'enseignement et de recherche français ou étrangers, des laboratoires publics ou privés.

Distributed under a Creative Commons Attribution 4.0 International License

High Temperature Corrosion of Materials (2024) 101:885–896
https://doi.org/10.1007/s11085-024-10267-6

ORIGINAL PAPER

Characterization of δ-PuGa (1 at%. Ga) Oxidation Under Dry Oxygen Atmosphere Exposure

N. Favart[1] · B. Ravat[1] · L. Jolly[1] · I. Zacharie-Aubrun[2] · P. Martin[3] · D. Menut[4] · I. Popa[5] · B. Oudot[1]

Received: 9 July 2024 / Revised: 11 July 2024 / Accepted: 17 July 2024 /
Published online: 20 August 2024
© The Author(s) 2024

Abstract

The oxidation of δ-stabilized plutonium alloy was studied under dry oxygen exposures for temperatures varying from 100 up to 300 °C and oxygen partial pressures varying from 10^{-4} up to 500 mbar. The coupling of X-ray diffraction, Raman spectroscopy and FIB-SEM has allowed to show that the oxide scale is composed of an outer layer of PuO_2 and an inner mixed layer of $\alpha+\beta$-Pu_2O_3 platelets propagating into a metallic zone corresponding to the stable phase of unalloyed Pu. Furthermore, the analysis of Pu oxidation kinetics has displayed first a parabolic growth governed by the diffusion of interstitial oxygen. This step consists of the thickening of the Pu_2O_3 layer with a decrease in α-Pu_2O_3 ratio in favor of β-Pu_2O_3. Then, a second step occurs consisting of a linear growth of the PuO_2-layer with the formation of thick nodules which tend to cover the whole oxide surface. Based on the results of this work, a general oxidation mechanism for δ-Pu alloy is provided.

Keywords Plutonium · Oxidation mechanism · Kinetics · Microstructure

✉ B. Ravat
brice.ravat@cea.fr

[1] CEA, centre de Valduc, 21120 Is-Sur-Tille, France

[2] CEA, centre de Cadarache, 13108 Saint-Paul-Lez-Durance, France

[3] CEA, centre de Marcoule, 30207 Bagnols sur Cèze, France

[4] Synchrotron SOLEIL, Ligne de Lumière MARS, L'Orme des Merisiers, Départementale 128, 91190 Saint Aubin, France

[5] ICB UMP 6303, CNRS Univ. Bourgogne Franche Comté, 9 avenue Savary, 21078 Dijon, France

Introduction

Plutonium is a radioactive element discovered in 1941 during the Manhattan project [1]. This is one of the most mysterious elements. Indeed, plutonium is located at the boundary between heavy and light actinides, leading to multiple peculiar properties. For instance, plutonium metal presents six distinct allotropic phases from room temperature up to its melting point (640 °C). Among these phases, δ-phase (f.c.c. structure) is the most relevant for metallurgic uses since it is the most ductile phase. As the δ-phase is stable at temperatures within the range 300 °C to 465 °C, Pu is usually alloyed with elements such as Al, Ga or Ce to stabilize the δ-phase at room temperature.

Plutonium and its alloys are very sensitive to oxidation [2, 3] which may be severe during long-term storage under an inadequately controlled atmosphere. Hence, plutonium oxidation has been widely studied since its discovery [4–6], but numerous points are still in discussion. Basically, it is known that oxidation in temperature under atmosphere containing oxygen leads to the formation of an oxide scale composed of an outer PuO_2 layer and a Pu_2O_3 inner layer. Pu sesquioxide exists in two different structures, α-Pu_2O_3 (cubic) and β-Pu_2O_3 (hexagonal). According to Gardner et al. [7], α-Pu_2O_3 would have a stoichiometry corresponding to $PuO_{1.52}$ while β-Pu_2O_3 would be the stoichiometric phase. According to Haschke et al. [8], α-Pu_2O_3 is considered to be the metastable form of β-Pu_2O_3. Moreover, the existence of intermediate oxides, as a homologous series Pu_nO_{2n-2}, has also been discussed by Ao et al. [9]. In addition, the presence of impurities such as carbon leads under specific conditions to the formation of a plutonium oxicarbide [10].

The oxidation kinetics of Pu and its alloys has also been studied in various experimental conditions. A 2-step kinetics process is commonly admitted. It consists of a parabolic step with the formation of a compact oxide layer, followed by a linear step with the occurrence of cracks in the oxide scale. Ravat et al. [11] have shown, by using in situ XRD analyses, that the parabolic growth results from the formation of Pu_2O_3, while the linear growth is exclusively induced by the growth of PuO_2. The influence of Ga, used as a δ-phase stabilizer element, on oxidation has also been investigated. Waber et al. [3] have shown that the presence of Ga seems to reduce the oxidation kinetics. It has also been shown by Ravat et al. [11] that the oxidation process leads to the destabilization of the δ-phase, with the occurrence of the allotropic phase of unalloyed Pu corresponding to the exposure temperature. Recently, Donald et al. [12] have evidenced the formation of a Ga-depleted layer beneath the oxide layer and have attributed the existence of this layer to a Ga diffusion mechanism from the alloy to form Ga_2O_3 at the oxide/gas interface. However, this formation of Ga_2O_3 has been disputed by Roussel et al. [13] based on XPS experiment results. Furthermore, according to the Reverse Monte Carlo analysis of EXAFS data performed by Ravat et al. [14], Ga seems instead to be incorporated into Pu substitution sites of PuO_2 lattice during oxidation. This result agrees with DFT calculations performed by Ao et al. and Hernandez et al. [15, 16]. The influence of O_2 partial pressure has also been

studied by Stakebake and Lewis [17]. The authors observed a threshold pressure temperature-dependent, below which the oxygen partial pressure has no influence on the kinetics. The authors have considered that this threshold pressure is associated with a mechanism change, from *n*-type to *p*-type. The microstructure of Pu oxides was also investigated by Donald et al. [18, 19]. Indeed, they have reported different morphological characteristics of oxide scale formed on PuGa alloys after exposures at room temperature under laboratory and wet air.

Despite numerous studies about the oxidation of Pu alloy, connections between the nature of the Pu oxides, the growth kinetics and the microstructure of the oxide layers still have to be better understood. This is the purpose of this paper which is a comprehensive study about the general mechanism of δ-Pu oxidation under oxygen in a wide range of temperatures. This work is based on experimental results obtained by using XRD analysis, Raman spectrometry and FIB-SEM.

This paper is organized as follow. First, details on the sample preparation, experimental devices specifically dedicated for Pu handling and methods are given. Then, the experimental results describing the microstructure and the composition of the oxide scale, the kinetics of the Pu oxide growth, the oxidation rate-controlling chemical species and the breakaway are addressed and discussed. In conclusion, a general oxidation mechanism is proposed.

Experimental Procedures

The studied alloy is a δ-PuGa 1 at.% fully homogenized through high temperature treatment of 1000 h at 460 °C under secondary vacuum. Samples have been machined and micro-cut in order to obtain two different shapes: either a disk of 15 mm diameter and 1.5 mm height, or parallelepiped ($7.5 \times 5 \times 1.5$ mm^3). All the samples were polished using SiC abrasive papers up to 4000 grade and then annealed for 10 min at 300 °C under secondary vacuum in order to recover the δ-phase destabilized during the sample preparation steps [10].

Samples have been oxidized either under 100 mbar of oxygen for temperatures varying from 100 °C up to 300 °C, or at 150 °C under oxygen partial pressure varying from 10^{-4} to 500 mbar. Exposures were carried out in a reaction chamber (TTK 450 Anton Paar) directly mounted on a θ/θ diffractometer (BRUKER AXS D8 Advance) located inside a glovebox. Diffraction patterns were recorded in situ during the exposure and have been analyzed using a modified Rietveld refinement method described in [11]. In addition, grazing incidence XRD analysis (E = 10 keV) was performed on oxidized samples, using a 2D Pilatus detector on the MARS beamline at the SOLEIL synchrotron facility. As this experiment was performed outside a glovebox, the samples were confined in a PMMA dome. Sealing was assured by a silicon ring and Kapton scotch. The PMMA dome was then inserted in a second dome in PEEK to ensure mechanical soundness.

SEM images of the sample surface were obtained using a FEG SEM (ZEISS SuPRA 40) placed in a glovebox. As the oxide layer is very brittle, cross sections were obtained by surface FIB milling (Ga^+ ion), using a current of 16 nA and 30 kV to remove the matter and then a current of 600 pA and 30 kV to have a clean surface.

Prior to FIB preparation, the samples have been covered by protective Au and Pt deposits. The latter has permitted to optimize FIB milling. This was performed in a ZEISS Auriga 40 equipped with a FIB column by Orsay physics.

Raman spectrometry analysis was carried out by using an iHR-320 Horiba spectrometer coupled via optical fibers with a confocal optical microscope located inside a glovebox [20]. The spectrometer was equipped with a green laser (532 nm wavelength) with a power of 18 mW. In order to avoid affecting the oxide layer, a filter was used to limit the laser power to 1.8 mW. The data have been analyzed with the Horiba Labspec6 software, equipped with a MCR (multivariate curve resolution) modulus.

Results and Discussion

Microstructure and Composition of the Oxide Scale

The different phases present during Pu oxidation were characterized by XRD. The diagram presented in Fig. 1 has been recorded on a sample oxidized for 37 h at 150 °C under 100 mbar O_2 and is representative of patterns recorded on all the samples exposed under partial oxygen pressures between 10^{-4} and 500 mbar and at temperatures between 100 and 200 °C. Three oxides were identified: the dioxide PuO_2 and the sesquioxides α-Pu_2O_3 (cubic) and β-Pu_2O_3 (hexagonal). Two phases related to the metal are observed: the δ-phase corresponding to the alloy, and the β-phase that is the stable phase of unalloyed Pu at this temperature. At higher temperatures, between 200 and 275 °C, the γ-phase, that is the stable phase of unalloyed Pu, appears instead of the β-phase. At 300 °C, there is no additional peak since the stable phase of unalloyed Pu is the δ-phase.

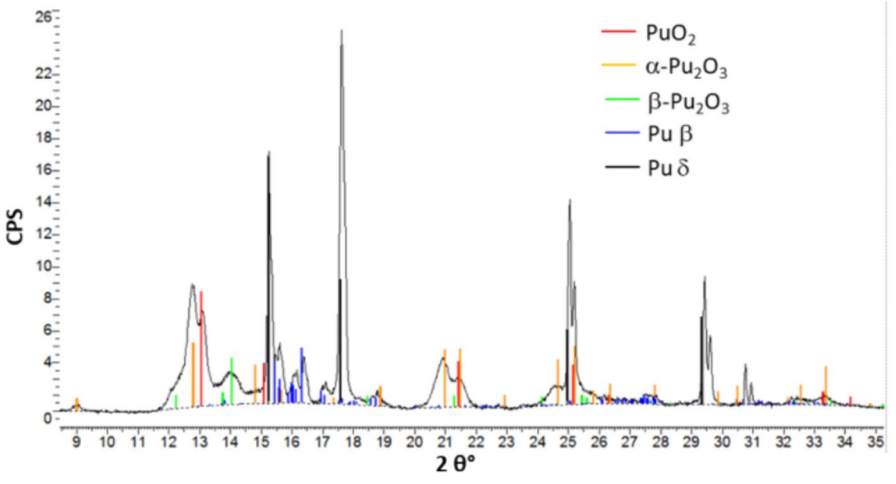

Fig. 1 XRD diagram of a sample oxidized 37 h at 150 °C under 100 mbar O_2

In order to characterize the arrangement of the phases in the oxide layer, an oxidized sample after an exposure during 80 h at 150 °C under 100 mbar O_2 was analyzed in grazing incidence XRD with incidence angles ω = 1° and 2°. As shown in Fig. 2, the diffraction peak at 2θ = 21.8° indicates the presence of PuO_2, while the peaks at 2θ = 21.4° and 2θ = 23.5° reveal the presence of α-and β-Pu_2O_3. The increase in the incidence angle corresponding to an increase in the oxide scale depth analysis leads to a decrease in the XRD peak intensities of PuO_2 and a rise of those corresponding to α-and β-Pu_2O_3. This behavior clearly shows that PuO_2 layer is located above Pu_2O_3. For both incidence angles, the concomitant observation and similar behavior of diffraction peaks related to α-and β-Pu_2O_3 demonstrate that both phases are mixed and do not form stacked layers. In order to investigate the spatial arrangement of the complex microstructure of α-and β-Pu_2O_3 phases, samples oxidized at 150 °C under 100 mbar O_2 with different exposure times (from 26 to 66 h) were characterized by using Raman spectroscopy using a × 50 objective. The variation as a function of depth of the oxide layer composition was studied by collecting Raman spectra at different z position respectively to the sample surface. Such depth scan was performed at several location of the samples. The spectra collected were analyzed by using the multivariate curve resolution (MCR) method. This analysis has highlighted 3 distinct components. One corresponds to the noise. Another component corresponding to the spectrum in red (Fig. 2b) exhibits a single band at 470 cm^{-1} which is characteristic of PuO_2 [21]. By deduction, the green spectrum corresponding to the last component which exhibits a few bands of low intensity is assigned to Pu_2O_3. Despite the numerous points analyzed, no specific spectrum separating the α- from the β-Pu_2O_3 was obtained.

To go further in the characterization of the oxide scale, a cross section of a sample oxidized for 240 h at 150 °C under 100 mbar O_2 was prepared by FIB milling. Underneath Au and Pt deposit layers, an oxide layer covering the whole surface of the sample with an average thickness between 2 and 3 µm can be seen in Fig. 3. In this oxide scale, different layers can be distinguished. The outer oxide layer is composed of PuO_2, in agreement with previous XRD analysis results. Underneath, there is an inhomogeneous layer of Pu_2O_3, that is around 1.6 µm thick. This layer is composed of platelets as revealed by the top view image (in the middle) obtained by reconstruction from

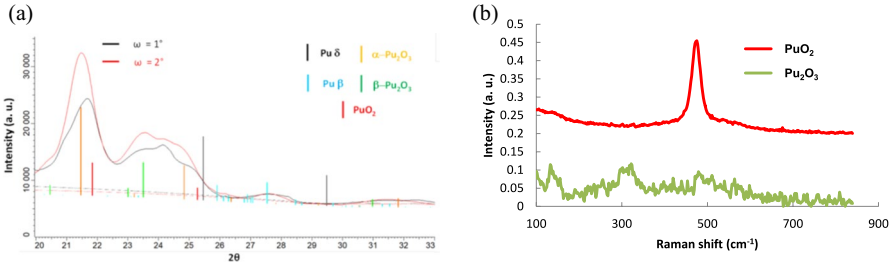

Fig. 2 Grazing incidence X-ray diffractograms of a sample oxidized 80 h at 150 °C under 100 mbar O_2 (**a**) and Raman spectra obtained on samples oxidized at 150 °C under 100 mbar O_2 for 26–66 h after MCR analysis of 36 Raman spectra (**b**)

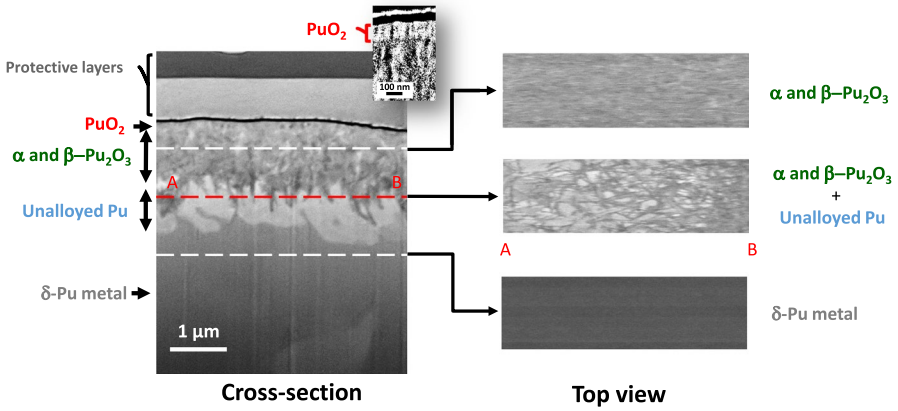

Fig. 3 SEM images of a FIB-milled cross section of the oxide scale of a sample oxidized for 240 h at 150 °C under 100 mbar O_2

SEM images of FIB-milled cross sections. They are 50 nm wide and at least 500 nm long. These platelets penetrate into a lighter layer, around 500 nm thick. This latter is assigned to the occurrence of an unalloyed Pu phase which is denser than the δ-phase. Its observation confirms the destabilization of the δ-phase which results from a depletion in Ga in the region of the alloy in contact with the oxide scale. During the oxidation process, as reported in [11–14], Ga would diffuse toward the oxide scale surface to form Ga_2O_3 or to be incorporated in Pu substitution sites in PuO_2 lattice.

Consequently, from grazing incidence XRD, Raman spectroscopy and FIB-SEM results, it can be concluded that the oxide scale is composed of an outer layer of PuO_2 located at the oxide/gas interface, and beneath, an inner mixed layer composed of platelets of (α+β)-Pu_2O_3 propagating into a metallic region corresponding to the stable phase of unalloyed Pu located above the δ-Pu alloy.

Kinetics of Pu Oxide Growth

Oxidation kinetics was studied by recording in situ and continuously XRD diagrams during exposure under oxygen. The thickness of each layer has been assessed by using modified Rietveld analyses [11]. However, in this previous work, the oxide scale was assumed to be a stacking of three distinct and successive layers of Pu oxides: PuO_2 on top, α-Pu_2O_3 in the middle and β-Pu_2O_3 underneath. In light of the results of this present work, a single mixed layer of α-Pu_2O_3 and β-Pu_2O_3 has to be taken into account. Consequently, the intensity correction functions used to refine the XRD peaks of α-and β-Pu_2O_3 were modified considering a mixed layer and are now expressed by the following relations:

$$k_{\alpha Pu_2O_3} = e^{\frac{-2\mu_{PuO_2} e_{PuO_2}}{\sin(\theta)}} * \left(1 - e^{\frac{-2x_{\alpha Pu_2O_3} \mu_{\alpha Pu_2O_3} e_{Pu_2O_3}}{\sin(\theta)}}\right) \quad (1)$$

$$k_{\beta Pu_2O_3} = e^{\frac{-2\mu_{PuO_2} e_{PuO_2}}{\sin(\theta)}} * \left(1 - e^{\frac{-2(1-x_{\alpha Pu_2O_3})\mu_{\beta Pu_2O_3} e_{Pu_2O_3}}{\sin(\theta)}}\right) \quad (2)$$

Figure 4a shows a typical oxidation kinetics, which first follows a parabolic and then a linear law. As already shown in [11], Pu_2O_3 is responsible for the parabolic growth, while PuO_2 is responsible of the linear growth. By considering the novel model of the microstructure of the oxide scale implemented in the Rietveld refinement, it can be noticed that the internal composition of Pu_2O_3 layer changes during both its thickening and the oxygen exposure time. Indeed, as shown in Fig. 4b, a decrease in the α-Pu_2O_3 ratio in favor of β-Pu_2O_3 occurs during the parabolic step. This suggests that α-Pu_2O_3 would form kinetically faster than β-Pu_2O_3 but would be metastable whereas β-Pu_2O_3 β-Pu_2O_3 could be the phase thermodynamically stable as suggested by Haschke et al. [8]. Nevertheless, it appears in this case that α-Pu_2O_3 remains the main oxide in the Pu_2O_3 layer although its concentration decreases until stabilizing at 70% at 150 °C.

In addition, the oxidation kinetics have been recorded for temperatures comprised between 100 and 300 °C. From these kinetics, parabolic growth rates k_p of the whole oxide layer and of the Pu_2O_3 layer have been determined separately. The k_p values, extracted from the linear regressions $e^2 = k_p \times t$, are represented in Fig. 5 in the form of an Arrhenius plot. It can be noticed that k_p values determined for the whole oxide scale and for Pu_2O_3 layer are very similar, confirming again the fact that Pu_2O_3 growth governs the parabolic step. Furthermore, k_p values determined in this study are lower by 10 order of magnitude in comparison with k_p values determined on pure Pu [22], highlighting the protective influence of Ga. The linear regression $\ln(k_p) = f(1/T)$ for the oxide layer and the Pu_2O_3 layer have, respectively, given the activation energy $E_{a(Pu_2O_3)} = 71.8$ kJ.mol^{-1} and $E_{a(tot)} = 72.2$ kJ.mol^{-1}. The small difference between these energies confirms that the growth of the Pu_2O_3 layer is responsible for the parabolic growth of the oxide layer.

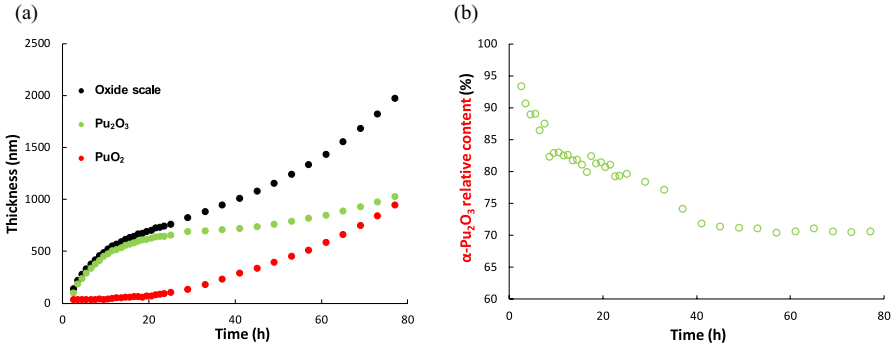

Fig. 4 Oxidation kinetics of a Pu–Ga 1 at.% sample at 150 °C under 100 mbar O_2 (**a**) variation of α-Pu_2O_3 ratio within the Pu_2O_3 layer as a function of exposure time

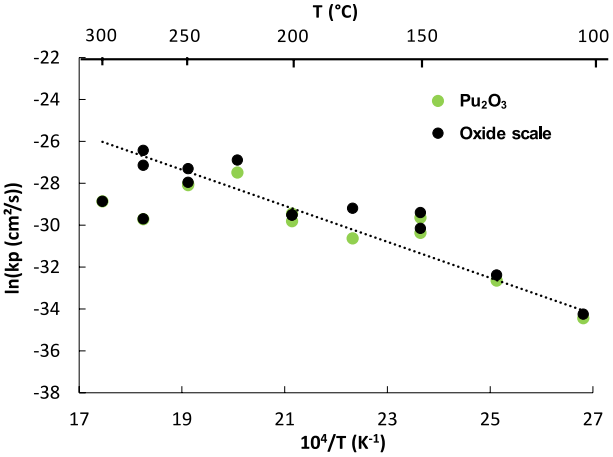

Fig. 5 Arrhenius plot of the parabolic rate constants determined for the whole oxide layer and for Pu_2O_3 layer grown under 100 mbar O_2 versus temperature

Oxidation Rate-Controlling Chemical Species

Another aim of this work was to determine the nature of the chemical species, which governs Pu oxidation during the parabolic kinetics step. Considering Wagner's oxidation theory, in case of a thick oxide layer growth (which is the case during parabolic growth of Pu–Ga 1at.% oxidation), the growth is driven by the diffusion of chemical defect through the oxide layer. There are four possible main defects which are: i) metal vacancy, ii) interstitial metal; iii) oxygen vacancy; and iv) interstitial oxygen. Each of these defects leads to different behaviors during the oxide growth. Metal vacancy and interstitial oxygen are characterized by an O_2 pressure dependence of parabolic constant rates, unlike interstitial metal and oxygen vacancy. Furthermore, anionic defects lead to an inward growth of the oxide layer, while cationic defects lead to an outward growth of the oxide layer. In order to determine the main defect during the parabolic growth step, oxidation kinetics at 150 °C under different

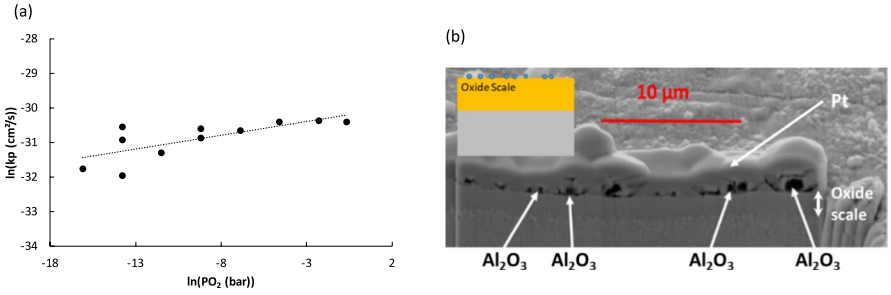

Fig. 6 Plot of k_p parabolic constants as a function of oxygen partial pressure at 150 °C (**a**), cross section SEM image of the oxide layer showing alumina remaining on top of the oxide scale (**b**)

O_2 partial pressures (from 10^{-4} to 500 mbar) were recorded. The k_p values are presented in Fig. 6a in the form $\ln(k_p) = f(\ln(P_{O_2})$. They show that the O_2 partial pressure has an influence on the parabolic growth rates indicating that the main defect is either interstitial oxygen or metal vacancy. To determine the oxide growth direction, an inert marker experiment was performed. Before high temperature exposure, the surface of a sample was covered with 100 nm alumina particles. After oxidation, as shown by the cross section (Fig. 6b), the alumina particles remain located on top of the oxide layer, indicating an inward growth of the oxide scale. Consequently, according to Wagner's oxidation theory, it can be deduced that the main defect is interstitial oxygen.

Breakaway

Oxidation kinetics analysis has shown the existence of breakaway related to a change in the kinetics growth mechanism. As shown in Fig. 7a, Pu_2O_3 lattice parameter increases during the parabolic growth step and goes down abruptly after the breakaway. This evolution of α-Pu_2O_3 lattice parameter indicates a stress accumulation in the Pu_2O_3 layer followed by a sudden relaxation. In the same time, the thickness of PuO_2 layer was constant and goes up quickly from the breakaway. Although breakaway was not fully reproducible in time, it seems to be connected to Pu_2O_3 thickness and exposure temperature. Indeed, Fig. 7b exhibits the necessary conditions (but not sufficient) to initiate the breakaway. The higher the exposure temperature, the thicker the Pu_2O_3 layer is at the breakaway. This observation suggests that there is a stress accommodation with increasing temperature that postpones the breakaway.

In addition, the sample surface at the different steps of the oxidation (parabolic growth, breakaway and linear growth) was characterized by SEM (Fig. 8). During the parabolic growth, the oxide surface is quite homogeneous and thin, and the metal grain boundaries are still apparent. Just after the breakaway, some oxide nodules are noticeable at the sample surface. These nodules are thick and porous, sizing from some dozens to some hundreds of square micrometers. Some of the nodules seem to be affected by spallation. By increasing the oxidation time, the

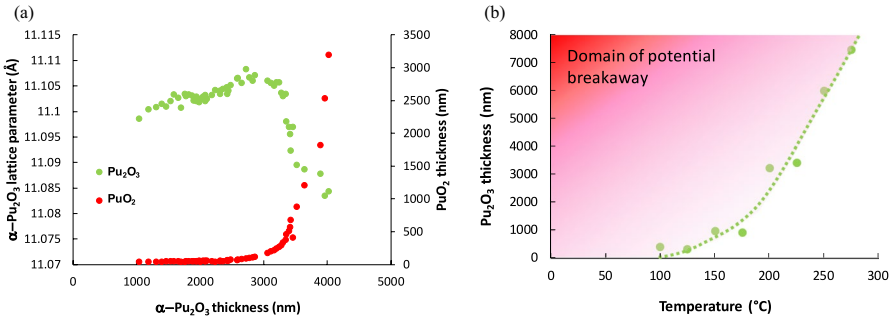

Fig. 7 Evolution of Pu_2O_3 lattice parameter and PuO_2 thickness during oxidation versus Pu_2O_3 layer thickness (**a**) Breakaway conditions as a function of Pu_2O_3 layer thickness and exposure temperature under 100 mbar O_2 (**b**)

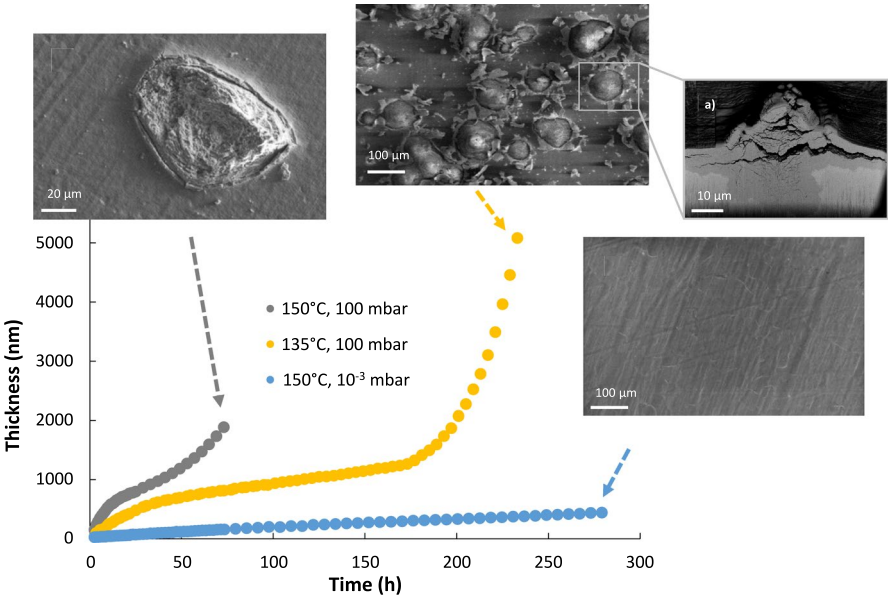

Fig. 8 SEM images of the oxide scale surface at different steps of the oxidation: parabolic growth, breakaway and linear growth

size and number of the nodules rise, covering more and more the surface of the sample. The cross section SEM image of this nodule reveals its microstructure. It is composed of a cracked external part of (15 µm high for the chosen nodule) and an internal part, below the surface, which goes very deeply inside the metallic substrate (about 20 µm in the considered example).

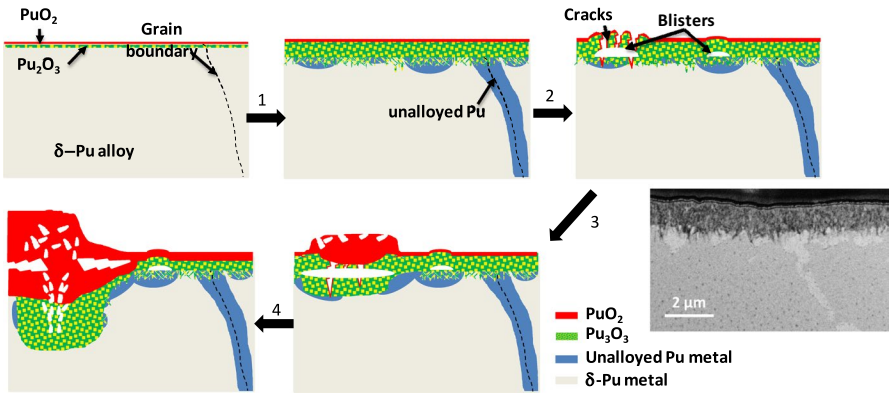

Fig. 9 Schematic representation of δ-Pu alloy oxidation mechanism during dry oxygen exposure at high temperature

Conclusion: Pu Oxidation Mechanism During Dry Oxygen Exposure

Based on the results of the present work, it is possible to propose a general oxidation mechanism schematized in Fig. 9. At the beginning of high temperature exposure, a "native" oxide scale, composed of PuO_2 and Pu_2O_3, is present at the Pu alloy surface. During exposure under oxygen atmosphere, a layer composed of platelets of α-and β-Pu_2O_3 phases grows following a parabolic law. Interstitial oxygen diffusion pilots this kinetics step. In the same time, the formation of allotropic phase of unalloyed Pu highlights the Ga diffusion through the oxide scale. As shown by the SEM image in Fig. 9, this diffusion can occur along the grain boundaries. The thickening of the Pu_2O_3 layer leads to the accumulation of stress. When the stress level overcomes the oxide scale strength, cracks and blisters appear at the surface leading to the linear growth step. Thick oxide nodules, likely composed of PuO_2, form in concomitance with the breakaway. The size and the number of these nodules are increasing with the exposure time. A porous oxide layer might result for longer exposures times, not tested in the present work. However, the occurrence of a porous layer and spallation have been already reported [11].

Author Contribution N. Favart and B. Ravat wrote the main manuscript. I. Zacharie-Aubrun, P. Martin, D. Menut, N. Favart L. Jolly and B. Ravat performed the experiments. I. Popa and B. Oudot reviewed the manuscript.

Funding Open access funding provided by Commissariat à l'Énergie Atomique et aux Énergies Alternatives.

Data Availability No datasets were generated or analyzed during the current study.

Declarations

Competing interest The authors declare no competing interests.

Open Access This article is licensed under a Creative Commons Attribution 4.0 International License, which permits use, sharing, adaptation, distribution and reproduction in any medium or format, as long as you give appropriate credit to the original author(s) and the source, provide a link to the Creative Commons licence, and indicate if changes were made. The images or other third party material in this article are included in the article's Creative Commons licence, unless indicated otherwise in a credit line to the material. If material is not included in the article's Creative Commons licence and your intended use is not permitted by statutory regulation or exceeds the permitted use, you will need to obtain permission directly from the copyright holder. To view a copy of this licence, visit http://creativecommons.org/licenses/by/4.0/.

References

1. S. S. Hecker, D. R. Harbur, and T. G. Zocco, *Progress in Materials Science* **49**, 429 (2004).
2. J. M. Haschke, T. H. Allen, and L. A. Morales, *Los Alamos Science* **26**, 252 (2000).
3. J. T. Waber, W. M. Olson, and R. B. Roof, *Journal of Nuclear Materials* **3**, 201 (1961).
4. T. D. Chikalla, C. E. McNeilly, and R. E. Skavdahl, *Journal of Nuclear Materials* **12**, 131 (1964).

5. J. M. Haschke, T. H. Allen, and L. A. Morales, *Journal of Alloys Compound* **314**, 78 (2001).
6. J. L. Stakebake, *Journal of Common Metals* **123**, 185 (1986).
7. E. R. Gardner, T. L. Markin, and R. S. *Journal of Inorganic and Nuclear Chemistry* **27**, 541 (1965).
8. J. M. Haschke, L. N. Dinh, and W. McLean, *Journal of Nuclear Materials* **458**, 275 (2015).
9. B. Ao and R. Qiu, *Corrosion Science* **153**, 236 (2019).
10. N. Favart, B. Ravat, L. Jolly, B. Oudot, L. Berlu, F. Delaunay, I. Popa, and S. Chevalier, *Oxidation Metals* **96**, 271 (2021).
11. B. Ravat, L. Jolly, B. Oudot, A. Fabas, H. Guerault, I. Popa, and F. Delaunay, *Corrosion Science* **138**, 66 (2018).
12. S. B. Donald, J. A. Stanford, W. A. Talbot, C. K. Saw, B. W. Chung, and W. McLean, *Corrosion Science* **194**, 109923 (2022).
13. P. Roussel, S. C. Hernandez, J. J. Joyce, K. S. Graham, and T. Venhaus, *Journal of Vacuum Science and Technology A* **41**, 023204 (2023).
14. B. Ravat, N. Favart, L. Jolly, D. Menut, B. Oudot, F. Delaunay, I. Popa, and S. Chevalier, *Corrosion Science* **218**, 111144 (2023).
15. B. Ao, R. Qiu, H. Lu, and P. Chen, *Computer Material Science* **122**, 263 (2016).
16. S. C. Hernandez and E. F. *The Journal of Physical Chemistry C* **120**, 13095 (2016).
17. J. L. Stakebake and L. A. Lewis, *Journal of the Less Common Metals* **136**, 349 (1988).
18. S. B. Donald and B. W. Chung, *Journal of Nuclear Materials* **547**, 152815 (2021).
19. S. B. Donald and B. W. Chung, *Journal of Nuclear Materials* **559**, 153473 (2022).
20. O. Kahraman, F. Lebreton, P. Martin, and M. Mermoux, *Journal of Applied Physics* **132**, 115106 (2022).
21. L. Medyk, D. Manara, J.-Y. Colle, D. Bouexière, J. F. Vigier, L. Marchetti, P. Simon, and Ph. Martin, *Journal of Nuclear Materials* **541**, 152439 (2020).
22. J. G. Schnizlein and D. F. Fischer, *Journal of The Electrochemical Society* **114**, 23 (1967).

Publisher's Note Springer Nature remains neutral with regard to jurisdictional claims in published maps and institutional affiliations.